

Property manipulated polypropylene–iron nanocomposites with maleic anhydride polypropylene

Jiahua Zhu,^{ab} Qingliang He,^a Zhiping Luo,^c Airat Khasanov,^d Yutong Li,^e Luyi Sun,^f Qiang Wang,^g Suying Wei^{*b} and Zhanhu Guo^{*a}

Received 16th April 2012, Accepted 1st June 2012

DOI: 10.1039/c2jm32371k

Magnetic polypropylene (PP) polymer nanocomposites (PNCs) were fabricated with the reinforcing core–shell Fe–Fe₂O₃ nanoparticles (NPs) synthesized by an *in-situ* thermal decomposition method. Maleic anhydride functionalized PP (M-PP) with two different molecular weights ($M_n = 800$, called LM-PP; $M_n = 8000$, called HM-PP) were found not only serving as surfactant to control the particle size, but also influencing the oxidation degree of the synthesized NPs. With regular PP only, the average nanoparticle size was 15.9 ± 2.2 nm. The NPs decreased to 10.6 ± 1.3 nm and 14.6 ± 2.7 nm in the presence of LM-PP and HM-PP, respectively. A surprisingly enhanced thermal stability by 117.6 °C in air was observed due to both the oxygen trapping effect of the NPs and the polymer–particle interaction. With only 2.4 wt% of M-PP in the PNCs, the complex viscosity was decreased by 86% at the frequency of 0.1 Hz. Enhanced saturated magnetization of the PNCs after introducing LM-PP indicated that the NPs were partially protected by the LM-PP shell and less dominated by the surface oxidation effects. The room temperature Mössbauer spectra analysis confirmed the oxidation degree of the NPs in each PNC and the molecular weight effect of M-PP on the restricted oxidation behavior of the NPs was studied as well. Both LM-PP and HM-PP change the crystalline fraction (X_c) of PP slightly (<1%) in the M-PP–PP blends. While in the PNCs, their contributions to the X_c of PP are significantly different from each other. Specifically, LM-PP increases the X_c of PP by 6.4% and HM-PP reduces the X_c by 10.1%. The electrical conductivity of these PNCs is also comparatively investigated.

1. Introduction

Iron group such as Fe, Co and Ni metallic nanoparticles (NPs) with small sizes are of great interest due to their high specific surface area, unusual magnetic properties such as large coercivity (H_c , a criteria to distinguish hard and soft magnetic materials)¹ and unique chemical catalytic properties.² Over the past decades, magnetic materials with various shapes, sizes and components have been designed and demonstrated wide potential

applications, for examples, in data storage,³ magnetic sensors,⁴ biomedical drug delivery⁵ and pharmaceutical areas.⁶ However, bare metal NPs are readily oxidized upon exposure to air/moisture, or even ignite spontaneously at room temperature.⁷ One approach is to coat the magnetic NPs with a protective shell and the reported shell materials include silica,^{8,9} polymer,¹⁰ carbon¹¹ and noble metals.^{12,13} Compared to the core–shell structure, the composite structure has demonstrated the same function as the core–shell structure to prevent oxygen diffusion through the thin polymer surrounding the metallic core NPs against their oxidation (anticorrosive coating for metal pipes and containers).¹⁴

Polymer nanocomposites (PNCs) or organic–inorganic hybrids attain the advantages of polymers such as light weight, easy processability and flexibility, and possess unique characteristics of the inorganic materials such as high mechanical strength, and excellent electrical, magnetic and optical properties,^{15,16} which are essentially different from those taken separately or physically combined individual components. For example, H_c of the magnetic NPs becomes larger after their dispersion in the hosting polymer matrix.¹⁷ These PNCs have attracted wide interest due to their diverse potential applications in energy storage devices,¹⁸ electronics¹⁹ microwave absorbers^{9,20} and sensors.³ Though many synthesis methods have been

^aIntegrated Composites Laboratory (ICL), Dan F. Smith Department of Chemical Engineering, Lamar University, Beaumont, TX 77710, USA. E-mail: zhanhu.guo@lamar.edu; Tel: +1 409 880-7654

^bDepartment of Chemistry and Biochemistry, Lamar University, Beaumont, TX 77710, USA. E-mail: suying.wei@lamar.edu; Tel: +1 409 880-7976

^cMicroscopy and Imaging Center, Texas A&M University, College Station, TX 77843, USA

^dUniversity of North Carolina at Asheville, Asheville, NC 28804, USA

^eMagnetic Head Operation, Western Digital Corporation, Fremont, CA 94539, USA

^fDepartment of Chemistry and Biochemistry, Texas State University—San Marcos, San Marcos, Texas 78666, USA

^gDepartment of Chemistry, University of Oxford, Mansfield Road, Oxford, OX1 3TA, UK

reported including solution blending,²¹ surface-initiated polymerization,²² melt blending²³ and *in-situ* polymerization,²⁴ there are still two main technical challenges for obtaining high-quality PNCs. One is the filler dispersion and the other is the polymer–nanofiller interaction. The agglomerated NPs will cause loss of advantageous nano-reinforcement and the obtained PNCs will behave as conventional composites with large fillers.²⁵ The poor bonding between the polymer matrix and the nanofillers, or even worse, the presence of voids will serve as crack initiating points and cause poor mechanical properties. Particle surface treatment/functionalization was normally used to improve the dispersion quality with proper surfactants, polymers and/or coupling agents.^{24,26,27} Good surface functional compatibility with the hosting polymer will favor the local stress being transferred from the weaker polymer to the stronger nanofillers for building high-performance structural materials.

Percolation threshold indicates the formation of long-range connectivity in a random system. In PNCs, percolation threshold stands for the critical value of the occupation probability that infinite connectivity of fillers first occurs. The criteria to use rheological characterization to evaluate percolation has been claimed and verified by several works.^{28,29} Other physical property changes of the PNCs are also observed at percolation. For example, the barrier properties of the polymer–clay nanocomposites have been remarkably improved due to the percolation of clay within the polymer matrix;³⁰ Barrau *et al.* observed glass transition temperature depression at the percolation threshold in the carbon nanotube–epoxy resin and polypyrrole–epoxy resin composites;³¹ A sharp change in mechanical strength³² and electrical conductivity³³ near the percolation threshold has been reported. Recently, Robbes *et al.*³⁴ reported an effective method that combines SAXS and TEM to determine the threshold of magnetic nanocomposites. This method can be appropriately used in the PNCs with a filler loading between 0.005 and 5 vol.%. However, it cannot be used in PNCs when the loading is beyond the range.

Polypropylene (PP), one of the most widely used thermoplastics with the advantages of excellent processability and low cost,^{35,36} has been processed into nanocomposites in the last few decades to improve its mechanical,²⁵ thermal,³⁷ crystallinity,³⁸ and electrical properties^{39,40} for exterior automobile parts, fire retardant materials and electrostatic discharge applications. However, neat PP is well known for its non-polarity and hydrophobicity with the specific hydrocarbon backbone structures, which exhibit poor affinity and adhesion to other materials such as polymers and organic–inorganic fillers. One alternative way to solve this problem is to graft polar groups, such as maleic anhydride (MAH) on the polyolefins.⁴¹ Especially for PP, MAH grafted PP (M-PP) has the similar main backbone structure as PP and can be used as a compatibilizer between PP and fillers to fabricate PP composites.⁴² The introduced M-PP may increase the interfacial area by creating entanglements on both sides of the interface, which lead to an improved compatibility between the polymer matrix and its filler. A protective M-PP layer could reduce oxidation and enhance compatibility between the protective layer on the particle surface and the polymer matrix. However, there rarely is a report on the magnetic PP nanocomposites,⁴⁰ especially in the presence of the MAH grafted PP (M-PP). In this paper, M-PPs were used to illustrate their

effects on the *in-situ* thermodecomposition synthesized particles. The effects of the molecular weight of M-PP on the physico-chemical properties of the M-PP–PP and the nanocomposites were investigated by selecting two different molecular weights. The specific component and oxidation degree of the prepared NPs were systematically characterized, including Mössbauer spectrum and magnetic hysteresis loops. The effects of M-PPs on the rheological properties, crystallinity, microstructure and thermal stability of the prepared PNCs were also presented through rheology, differential scanning calorimetry, transmission electron microscopy and thermal gravimetric analysis. The magnetic properties of the different PNCs were also studied and compared.

2. Experimental

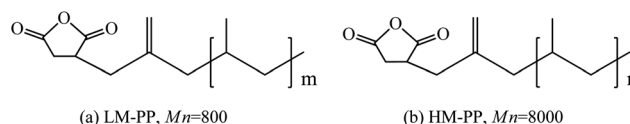
2.1. Materials

The isotactic polypropylene (PP) used in this study was supplied by Total Petrochemicals USA, Inc ($\rho = 0.9 \text{ g cm}^{-3}$, $M_n \approx 40\,500$, $M_w \approx 155\,000$, melt index $\approx 35 \text{ g min}^{-1}$). The maleic anhydride functionalized PP (M-PP) with two different molecular weights (LM-PP, $M_n \approx 800$, $\rho = 0.85 \text{ g cm}^{-3}$; HM-PP, $M_n \approx 8000$, $\rho = 0.90 \text{ g cm}^{-3}$) was supplied by Baker Hughes Company. Both LM-PP and HM-PP with a maleic anhydride group grafted to one end of the polymer chain have a similar PP backbone structure. Scheme 1 shows the chemical structure of the used M-PP. Iron(0) pentacarbonyl ($\text{Fe}(\text{CO})_5$, 99%) was commercially obtained from Sigma Aldrich. Solvent xylene (laboratory grade, $\rho = 0.87 \text{ g cm}^{-3}$) was purchased from Fisher Scientific. All chemicals are used as-received without any further treatment.

2.2. Preparation of polymer nanocomposites

The typical procedures for fabricating M-PP–PP blends and PNCs are as follows. Firstly, PP (20.0 g) and M-PP (0.5 g) were initially dissolved in xylene (207 mL) and refluxed at $\sim 140 \text{ }^\circ\text{C}$ for 2 h. Then $\text{Fe}(\text{CO})_5$ (17.48 g) was injected into the mixture solution to obtain a calculated iron weight ratio of 20 wt%. The mixture solution turned from transparent to yellow immediately after the addition of $\text{Fe}(\text{CO})_5$ and then gradually changed to black during the refluxing process for additional 3 h. The PNC solution was then cooled down to around $90 \text{ }^\circ\text{C}$ and then poured onto a large glass plate to allow the solvent evaporation overnight. The powder-like products were collected and dried in a vacuum oven at room temperature overnight. M-PP–PP blends were prepared following the same procedures without adding $\text{Fe}(\text{CO})_5$. The PNCs without M-PP were also prepared for comparison.

The desired samples were fabricated from the as-prepared powders using a hot press (Carver 3853-0, USA). Briefly, the powders were compressed in a cylinder-shaped mold under the



Scheme 1 Chemical structure of the (a) LM-PP and (b) HM-PP.

pressure of 10 MPa and heated to 180 °C at a heating rate of 20 °C min⁻¹. The compressed composites were held at 180 °C for 20 min and then cooled to ambient temperature in the mold while maintaining the pressure unchanged. For melt rheology testing, the sample was machined into a pellet shape with a diameter of 25 mm and a thickness of 2–3 mm.

2.3. Characterization

The powder X-ray diffraction (XRD) analysis on the pellet-shaped samples was carried out with a Bruker AXS D8 Discover diffractometer with a general area detector diffraction system (GADDS) operating with a Cu-K α radiation source filtered with a graphite monochromator ($\lambda = 1.5406 \text{ \AA}$). The detector used was a HISTAR two-dimensional multi-wire area detector. The samples were mounted on a quarter-circle Eulerian cradle (Huber) on an XYZ stage. The X-ray beam was generated at 40 kV and 40 mA power and was collimated to about an 800 μm spot size on the sample. The incident ω angle was 5°. A laser/video system was used to ensure the alignment of the sample position on the instrument center. XRD scans were recorded from 10 to 30° for 2θ with a 0.05° step-width and a 60 s counting time for each step.

The particle distribution in the PP matrix was examined using a transmission electron microscope (TEM). The samples were stained in RuO₄ vapor to harden the surface and microtomed into a film with a thickness of $\sim 100 \text{ nm}$, which was observed in a JEOL 2010 TEM at a working voltage of 200 kV. Images were recorded with a Gatan Orius SC 1000 CCD camera. In order to obtain more accurate particle size, magnifications were calibrated using a commercial cross-line grating replica and SiC lattice images.⁴³

The Mössbauer spectrometer was set to produce a high precision Doppler velocity modulation of the source γ radiation. The effects of the Doppler velocity modulation on the absorption of γ radiation were recorded synchronously in the 1024 channels of the multichannel analyzer. The result was 1024 numbers representing registered gamma quanta (representing a singular quantum) passing through the absorber under the conditions of different Doppler velocity. A separate calibration procedure establishes the exact correspondence channel-velocity (the spectrometer calibration is performed by measuring a standard α -Fe absorber, which produces a well known six-line spectrum. The whole velocity range is calibrated using these six velocity points. Naturally, any shifts in the spectra using this calibration are reported with respect to the zero point of α -Fe spectrum). The shape of the absorption spectrum was fitted to a theoretical model line shape, which was a superposition of singlets, doublets and sextets (57Fe case) of a Lorentzian form. This was done with the aid of specialized computer programs. The result was investigated by chi 2 criterion and the theoretical line shape is tailored to fit the experimental spectrum by adjustment of the spectral parameters like isomer shift, quadrupole splitting, hyperfine magnetic field, etc.

The rheological behavior of pure PP, M-PP-PP blend and their corresponding PNC melts was studied using an AR 2000ex Rheometer (TA Instruments). An ETC steel parallel-plate geometry (25 mm in diameter) was used to perform the measurement at 200 °C, with dynamic oscillation frequency

sweeping from 100 to 0.1 Hz in the linear viscoelastic range (LVR with a used strain: 1%) under nitrogen atmosphere.

The thermal degradation of pure PP, M-PP-PP blends and their PNCs was studied using a thermo-gravimetric analysis (TGA, TA instruments Q-500) from 25 to 600 °C in air and nitrogen atmosphere, respectively, with a flow rate of 60 mL min⁻¹ and a heating rate of 10 °C min⁻¹. Differential scanning calorimetry (DSC, TA Instruments Q2000) measurements were carried out under a nitrogen flow rate of approximately 100 mL min⁻¹ at a heating rate of 10 °C min⁻¹ from 0 to 250 °C.

The magnetic property measurements of the PNCs were carried out in a 9 T physical properties measurement system (PPMS) by Quantum Design at room temperature.

The volume resistivity was determined by measuring the DC resistance on a disk-shaped sample (diameter, 25 mm; thickness, $\sim 1.0 \text{ mm}$). An Agilent 4339B high resistance meter equipped with a resistivity cell (Agilent, 16008B) was used to measure the volume resistivity of each sample after inputting the thickness. This equipment allows a resistivity measurement up to 10¹⁶ Ω . The source voltage was set at 0.1 V for all the samples. The reported values represent the mean value of eight measurements with a deviation less than 10%.

3. Results and discussion

3.1. Crystalline phase and microstructures of the nanocomposites

The crystallinity of the pure PP, LM-PP, HM-PP and the corresponding PNCs is investigated using X-ray diffraction, Fig. 1. Despite the simplicity of its chemical component, PP shows remarkable complexity of crystal structures (phases), which include α , β , and γ phases. Each of the α , β , and γ crystalline forms has its own distinctive peaks in the XRD patterns. In a typical XRD pattern of the α phase PP, the intensity of the first peak (110) is always stronger than that of the second peak (040).⁴⁴ However, it is not true for the samples containing γ phase. All samples are characterized by a second peak (040) stronger than that of the first one (110), which is not surprising considering the same location of the strong peak in the γ phase.

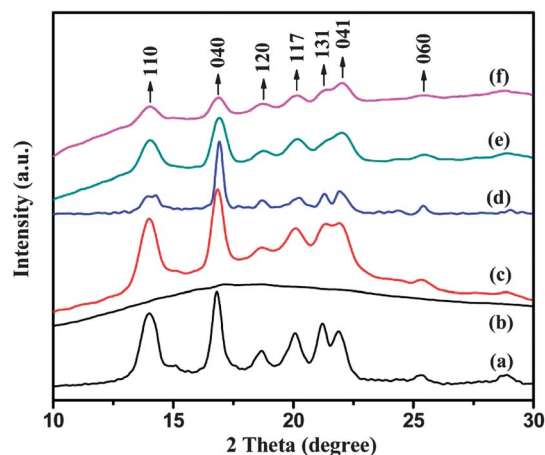


Fig. 1 (a) PP, (b) LM-PP, (c) HM-PP, (d) NPs-PP, (e) NPs(LM-PP)-PP and (f) NPs(HM-PP)-PP.

Because of the high diffraction similarity between α and γ phases in the region of $13\text{--}17^\circ$, the γ phase is usually determined from the peak at $2\theta = 20.1^\circ$ (117), and the α phase is identified from the peak at $2\theta = 18.5^\circ$ (120).⁴⁵ The other peaks at $2\theta = 14.1, 16.9, 21.2, 21.9$ and 25.4° correspond to the 110, 040, 131, 041 and 060 crystalline planes of α -PP, respectively.⁴⁵ All curves show a similar XRD pattern except for the LM-PP, which exhibits an amorphous nature due to the low molecular weight. Similar peaks were observed from PP and HM-PP that both curves present a combination of α and γ crystal phases. The only difference between these two curves comes from the relative intensity of the peaks at 21.2° (131) and 21.9° (041), both peaks come from the α -PP. The PP gives a higher (131) peak intensity than that of (041), while the HM-PP shows an equal intensity of these two peaks. It is interesting to observe that the peak intensity of (041) exceeds the (131) peak intensity in the PNCs especially those with LM-PP and HM-PP, while the other peaks kept the same characteristics as compared to PP. This phase behavior is related to the formed NPs in the PNCs and the LM-PP (HM-PP) promotes this change with regard to these two crystal phases as evidenced by the higher intensity of the (041) peak in the PNCs.

The nanoparticle dispersion and identification are characterized by TEM observations and Mössbauer spectra, Fig. 2 and 3, respectively. The *in-situ* formed NPs have size 10–15 nm and

appear in the form of fractal aggregates, which are observed to form an interconnected network structure, Fig. 2(a–c). After introducing LM-PP and HM-PP, the crystalline structure of the NPs is improved as evidenced by the clear selected area electron diffraction (SAED) rings, Fig. 2(d–f).⁴⁶ The size distribution and the average diameter of the NPs are compared, Fig. 2(g–i). The NPs synthesized with the addition of M-PP tend to become smaller than the NPs (15.9 ± 2.2 nm) prepared in the presence of the regular PP. Furthermore, the molecular weight of M-PP was observed to have a significant impact on the particle size. Specifically, 10.6 ± 1.3 nm is observed in the NPs synthesized with the addition of LM-PP ($M_n \approx 800$) and the NPs become relatively larger (14.6 ± 2.7 nm) with the addition of HM-PP ($M_n \approx 8000$). Previous studies reveal that a small mass ratio of bulk chains/grafted chains should cause widening of the region where the grafted polymers are stretched and completely wetted,^{47,48} in which the HM-PP should be able to acquire a higher grafting density. However, this work is different from previous studies, which were based on the homogeneous polymers. First of all, MAH functional groups have been grafted to the head of M-PP, Scheme 1, which allow them to be strongly bonded to the nanoparticle surface and leave the PP tails behind. Therefore, the mass ratio dependent wetting/dewetting behavior is less effective in the current study. The steric hindrance does not

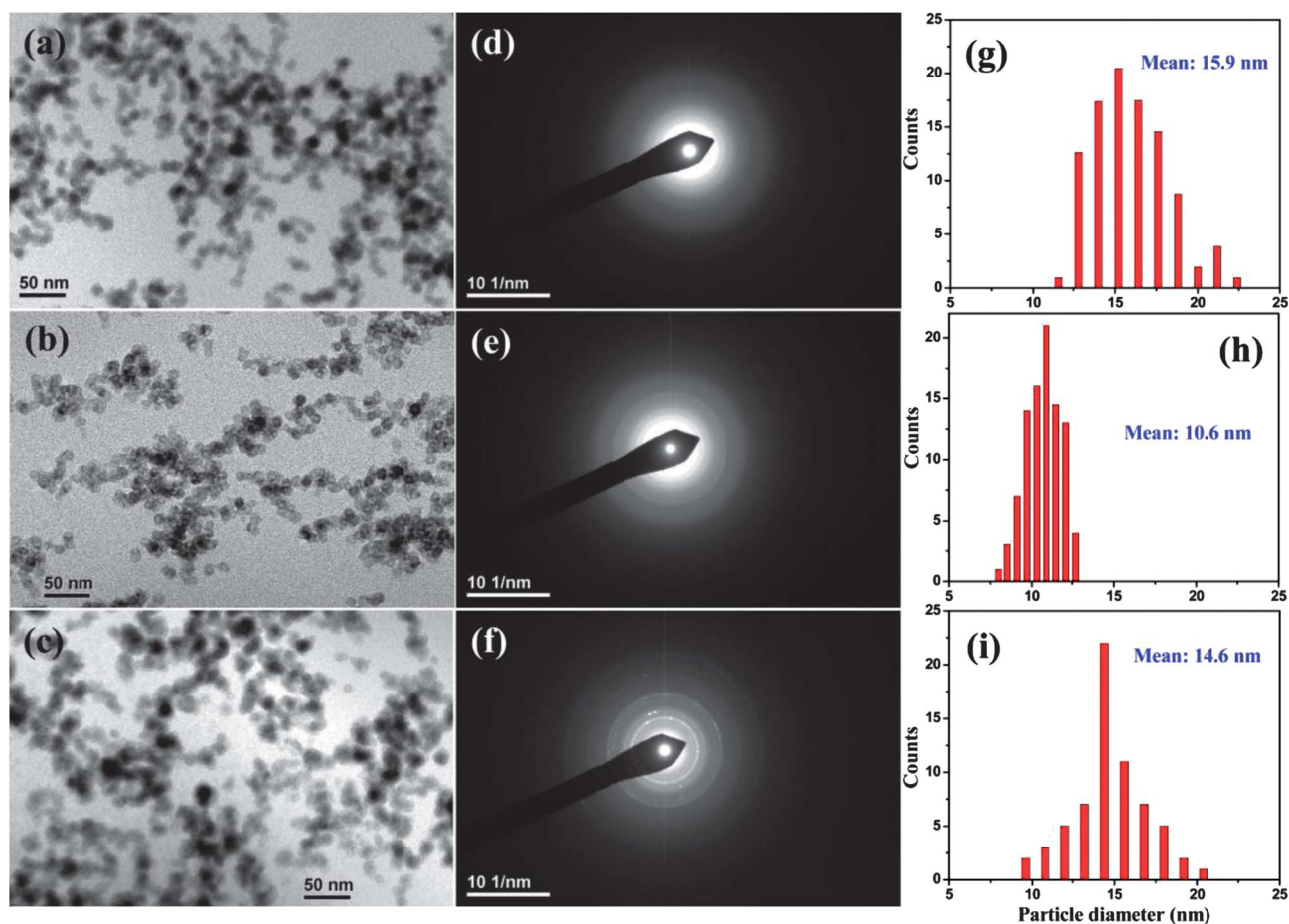


Fig. 2 TEM images of (a) NPs–PP, (b) NPs(LM-PP)–PP and (c) NPs(HM-PP)–PP. (d–f) and (g–i) corresponding to the electron diffraction pattern and particle size distribution of (a–c), respectively.

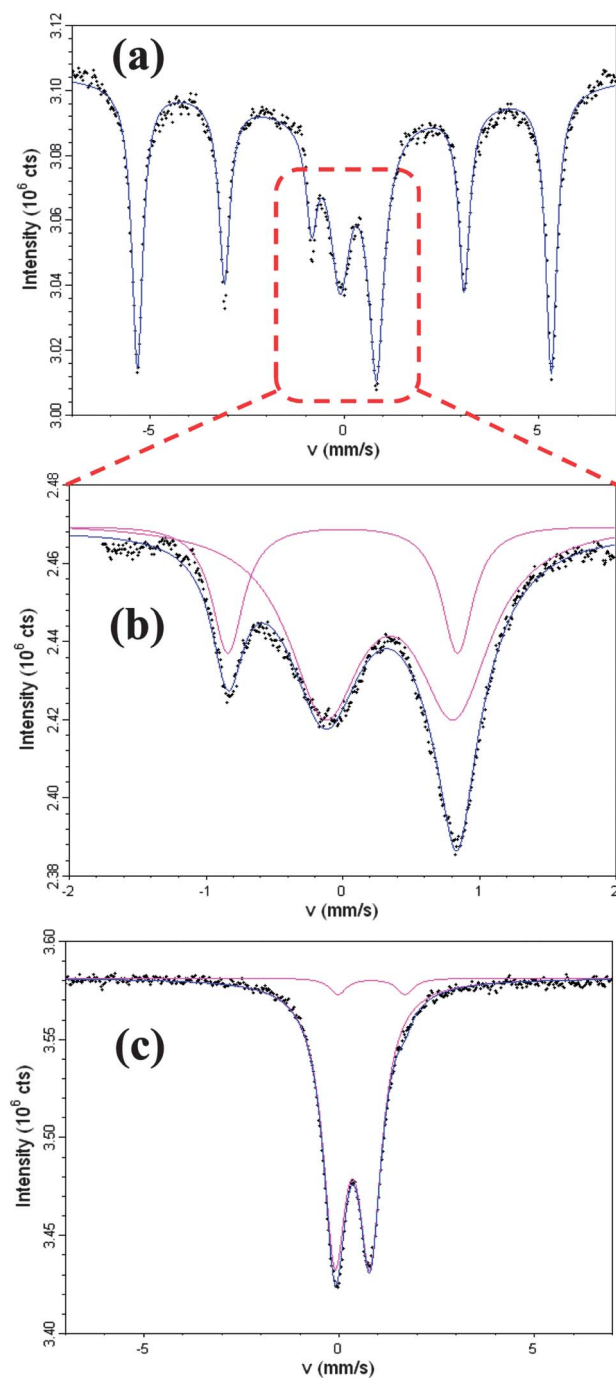
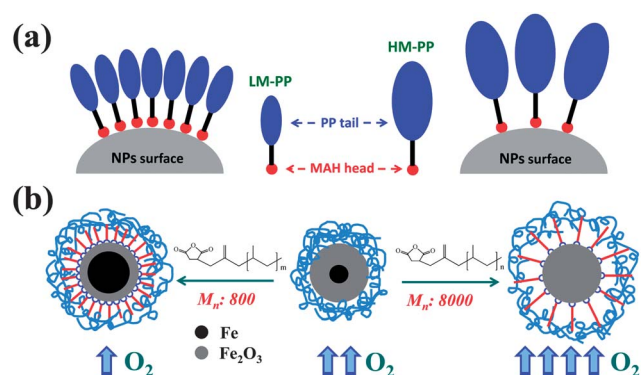


Fig. 3 Mössbauer spectrum of (a) NPs(LM-PP)-PP, (b) enlarged spectrum of NPs(LM-PP)-PP from -2 to 2 mm s^{-1} and (c) NPs(HM-PP)-PP.

arise from the interaction between the bulk PP chain and the M-PP grafted NPs. On the contrary, it is from the size of the PP tails, Scheme 2. The larger the molecular weight of the M-PP, the larger the size of the PP tail will be. Therefore, higher packing density of LM-PP on the nanoparticle surface is expected due to the short polymer chain ($M_n \approx 800$) and less steric hindrance.⁴⁹ The nuclei diffusion would be significantly limited with the corona LM-PP chain bonding on the particle surface and thus a smaller size of the NPs was observed in the HM-PP grafted NPs as compared to LM-PP grafted NPs.



Scheme 2 (a) Schematic grafting of LM-PP and HM-PP on the nanoparticle surface with high packing density of LM-PP and low packing density of HM-PP, and (b) Schematic illustration of the synthesized NPs embedded in LM-PP-PP, PP and HM-PP-PP (from left to right) as well as the oxygen penetration behavior into these PNCs (the drawing is not scaled).

The room-temperature Mössbauer spectra of NPs(LM-PP)-PP PNCs show a combination of one paramagnetic doublet in the center and one magnetically split sextet pattern, Fig. 3(a and b). The fitting results show the main component at isomer shift (IS) = 0 mm s^{-1} and the corresponding HI = 330 kOe, which represents a spectral contribution of 67% metallic iron in the magnetically ordered state. Fig. 3(b) depicts the secondary component (33%) with IS = 0.35 mm s^{-1} , quadrupole splitting (QS) = 0.91 mm s^{-1} , which is Fe^{3+} in a paramagnetic state in the distorted oxygen octahedral site. The paramagnetic doublet observed in the center of the Mössbauer spectrum corresponds to the superparamagnetic behavior of Fe_2O_3 at room temperature.⁵⁰ The Mössbauer spectrum of NPs(HM-PP)-PP PNCs, Fig. 3(c), shows two paramagnetic doublet patterns consisting of a major component of Fe^{3+} (96%) with IS = 0.34 mm s^{-1} , QS = 0.90 mm s^{-1} , and Fe^{2+} (4%) as the secondary component with IS = 0.83 mm s^{-1} , QS = 1.72 mm s^{-1} . This observation indicates that iron was completely oxidized in the case of HM-PP stabilized PNCs. A similar doublet pattern consisting of 95% Fe_2O_3 and 5% α -Fe was observed in the NPs-PP PNCs.⁴⁰ These comparison investigations demonstrate that the molecular weight of the M-PP plays a significant role in determining the chemical composition of the synthesized NPs. Scheme 2(a) shows the grafting of LM-PP and HM-PP on the nanoparticle surface, the MAH functional groups have been covalently bonded to the NP surface leaving the PP tails behind along the radial direction of the NPs. The larger PP tail of HM-PP introduces significant steric hindrance on the nanoparticle surface and thus a lower packing density would be expected, which leaves more free volume at the PP-NPs interface facilitating the oxygen penetration. The oxygen penetration behavior in different PNCs and their corresponding effect on the oxidation degree of the NPs are illustrated in Scheme 2(b). With a compact LM-PP grafting layer, less uncovered area of the NPs is exhibited at the interfacial area and thus the NPs would be better protected from oxidation which is consistent with the observed less fraction of iron oxide in the NPs revealed by the Mössbauer spectrum, Fig. 3.

3.2. Melt rheology

Fig. 4 shows the complex viscosity (η^*) of the melts of pure PP, M-PP-PP blends and their corresponding PNCs with different compositions at 200 °C. Both pure PP and M-PP-PP blends with a constant η^* at lower frequency indicate a Newtonian-type flow. The η^* decreases with increasing the frequency, indicating the presence of the shear thinning behavior.^{27,40,51} The HM-PP-PP blend melts exhibit a relatively higher η^* value than the LM-PP-PP and HM-PP melt samples within the whole frequency range from 0.1 to 100 Hz. The observed slightly larger η^* of the HM-PP-PP blends than that of pure PP is due to the strong polymer chain entanglement between pure PP and HM-PP.^{52,53} The HM-PP is able to entangle with the PP chains due to the same backbone structure with extended length. This entanglement would definitely introduce internal friction between HM-PP and PP chains during oscillation,⁵² which therefore results in an enhanced η^* . For LM-PP-PP blends, the polymer chain entanglement between LM-PP and PP chains is less effective due to the short polymer chain length of LM-PP and thus a similar η^* is observed as compared to that of pure PP.

The η^* is observed to increase by orders of magnitude after incorporating the NPs, which is due to the significant increase of the storage modulus G' and loss modulus G'' ($\eta^* = \eta' - i\eta''$, where $\eta' = G'/\omega$, $\eta'' = G''/\omega$, ω is the angular frequency, Hz)⁵⁴ arising from the local confinement of the NPs on the polymer chains.²⁷ The PNCs without M-PP exhibit significantly larger η^* than that of the PNCs with M-PP, especially at low frequencies. For example, the η^* value of the NPs-PP is about 6 times larger than that of NPs(LM-PP)-PP and NPs(HM-PP)-PP PNCs at 0.1 Hz. The LM-PP and HM-PP are favorably bonded to the NPs due to the reactive MAH group and are pre-melted before the melting of PP matrix, Table 1. Meanwhile, the less viscous LM-PP-HM-PP layer serves as a lubricant layer and prevents strong interaction between NPs and PP chains. For NPs-PP, the NPs-PP interfacial interaction still exists at high temperature due to the strong affinity between the NPs and PP chains,^{40,55} which well explains the significantly reduced η^* in the NPs(LM-PP)-PP

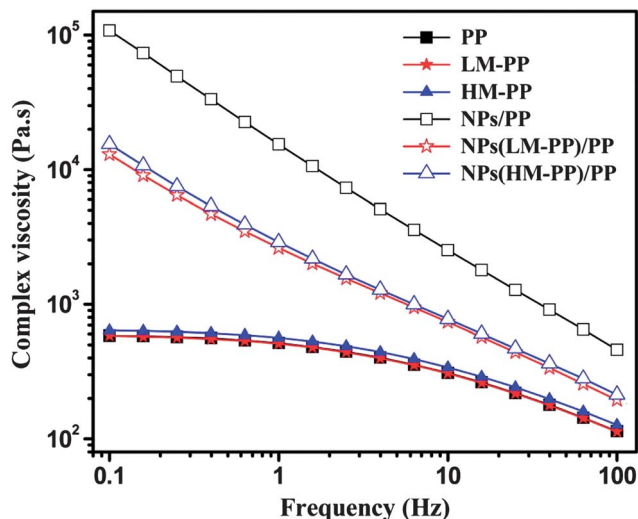


Fig. 4 Complex viscosity of pure PP, M-PP-PP blend and PNC melts at 200 °C. The PP and LM-PP curves are nearly overlapped.

Table 1 DSC characteristics of the measured samples^a

Composition	T_m (°C)	ΔH_m (J g ⁻¹)	T_c (°C)	ΔH_c (J g ⁻¹)	X_c (%)
Pure PP	149.2	90.4	119.5	88.6	43.3
LM-PP	—	—	—	—	—
HM-PP	136.8	88.9	104.1	91.4	42.5
LM-PP-PP	144.8	90.0	102.7	83.5	44.1
HM-PP-PP	149.5	91.2	118.4	84.6	43.6
NPs-PP	150.8	71.9	102.3	70.4	44.4
NPs(LM-PP)-PP	146.6	79.2	103.6	73.2	50.8
NPs(HM-PP)-PP	145.1	54.3	104.4	51.4	33.3

^a The weight fraction of the LM-PP, HM-PP and NPs is excluded to calculate the X_c of PP. For the HM-PP and NPs(HM-PP)-PP, the contribution of the enthalpy from HM-PP is subtracted according to the actual weight fraction.

and NPs(HM-PP)-PP PNCs. Most importantly, the viscosity is a critical parameter in polymer processing. High viscosity makes the processing and manufacturing a big challenge or even impossible. Therefore, the small amount of M-PP in the PNCs greatly facilitates the processing of PNCs. A more intense shear thinning phenomenon was observed in the PNC melts even at low frequency. The almost linear viscosity curve within the whole frequency range indicates filler-dominated fluid behavior in the PNC melts with a relatively high particle loading. In addition, the linear increase of η^* with decreasing shear frequency of the PNC melts at low frequency indicates the presence of a yield stress. This yield phenomenon was observed in the phase-separated multicomponent polymer blends due to the formation of a network structure from the dispersed blend components, which was originally proposed by Müntstedt⁵⁶ from the rheological studies of acrylonitrile butadiene styrene (ABS) resins with varying butadiene contents, and later on Utracki and Sammut also observed this yielding phenomenon in polystyrene-polyethylene⁵⁷ and polycarbonate-polyethylene⁵⁸ blends. More recently, the yield phenomenon has been observed in organo-clay-Nylon 6 (ref. 59) and layered silicate-poly lactide PNCs.⁶⁰ The rheological network structure of the NPs in PP has been constructed at a loading of 3.4 wt% (ref. 40) (the loading of 20 wt % in the current PNCs is far beyond percolation and thus the network structure has formed), which well explains the observed yield phenomenon in the PNCs.

Fig. 5 shows the storage modulus (G'), loss modulus (G'') and $\tan \delta$ as a function of frequency for the melts at 200 °C. G' increases significantly with the addition of NPs, Fig. 5(a). Large enhancement of the G' with orders of magnitude is observed at lower frequencies, indicating that the large-scale polymer chain relaxation in the PNCs is dramatically restrained by the presence of the NPs.⁴⁰

The G' curve of the PNC melts approaches a “plateau” at low frequencies, which suggests an interconnected structure of the nanofillers or a strong interaction between the filler and polymer.⁶¹ This result is in good agreement with the observation of η^* at low frequency and a similar low frequency response was also observed in the montmorillonite-poly(ϵ -caprolactone) and montmorillonite-nylon-6 PNCs⁶² and carbon nanotube-poly(methyl methacrylate) PNCs.⁶³ It is worth noting that the NPs(HM-PP)-PP PNC melts show the G' value an order of

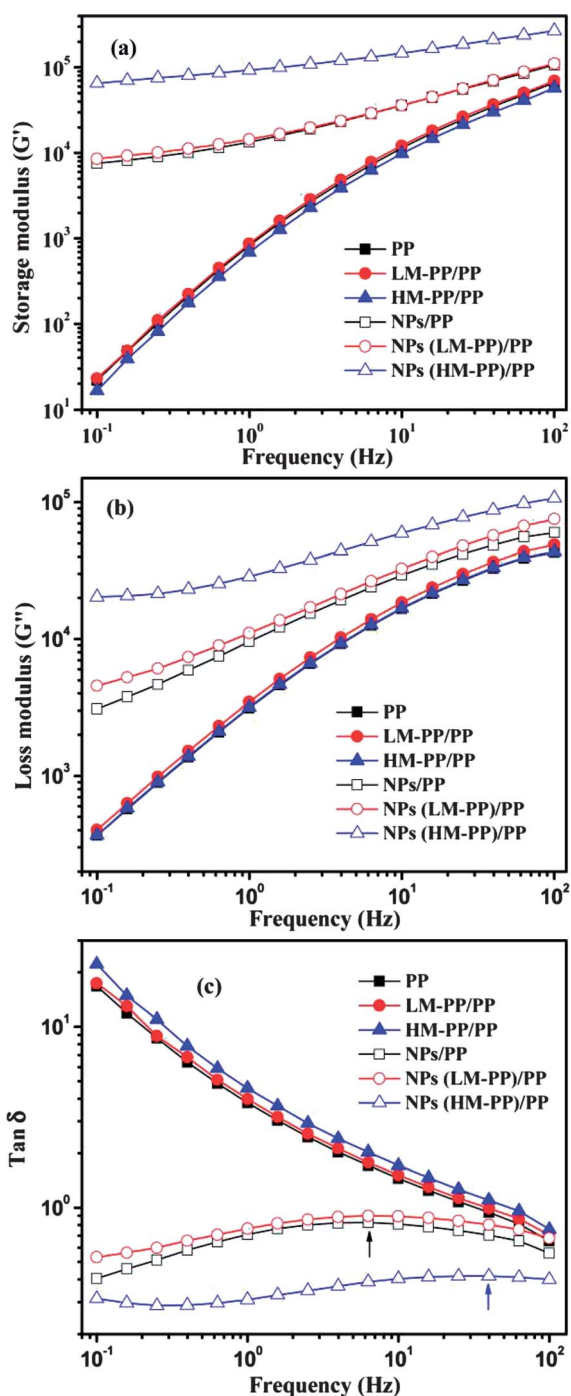


Fig. 5 (a) Storage modulus (G'), (b) loss modulus (G'') and (c) $\tan \delta$ of pure PP, M-PP-PP blend and PNC melts at 200 °C.

magnitude higher than that of NPs(LM-PP)-PP PNCs at a frequency of 0.1 Hz. With the MAH functional group covalently bonded to the nanoparticle surface, the long backbone PP chain of the HM-PP provides the advantage of chain-chain entanglement between HM-PP and PP chains. Thus, strong interactions of the two phase materials are obtained and the PNCs exhibit more obvious viscoelastic behavior as evidenced by the larger G' . On the contrary, the LM-PP can not entangle with the PP chains efficiently owing to its short backbone PP chain length and thus only slight enhancement of G' was observed in the

NPs(LM-PP)-PP PNC melts than that of the NPs-PP PNC, Fig. 5(a). Similar curves of the G'' with increasing frequency are observed, Fig. 5(b).

The $\tan \delta$ is the ratio of G'' and G' , which is used to characterize the damping behavior of the PNCs. It is obvious that the $\tan \delta$ decreases and the corresponding curves become flatter with incorporation of NPs in PNCs, Fig. 5(c). The mechanical loss, which arises from the discordance between strain and stress in the polymer exposed to an external force, is strongly related to the applied frequency. The $\tan \delta$ of pure PP and M-PP-PP blend melts decreases monotonously, while a broad peak is observed in all PNC samples. The higher $\tan \delta$ of pure PP than that of the PNCs is due to the full relaxation of the PP chains, which makes the interchain motion more difficult and thus more interchain friction heat is generated during oscillation. After incorporating the NPs, the polymer chain relaxation and relative motion have been greatly restrained by the presence of the NPs and the PNCs are "stiffer". Therefore, less internal chain-chain friction heat is produced upon applying the same oscillation frequency. Comparing the PNCs with/without M-PP, the $\tan \delta$ peak of NPs(HM-PP)-PP shifts to higher frequency due to the greater restrictions. Similar phenomena have been observed in the carbon nanofiber-PP PNCs.⁶⁴

3.3. Thermal stability and polymer phase microstructure of the nanocomposites

Fig. 6 shows the thermal decomposition curves of pure LM-PP and HM-PP from room temperature to 600 °C under air and nitrogen atmosphere, respectively. Both LM-PP and HM-PP decompose at higher temperature in nitrogen than in air atmosphere due to the larger activation energy of random scission from thermal degradation than that of oxidative degradation, which is consistent with the observation in poly(methyl methacrylate).⁶⁵ However, it is interesting to observe that HM-PP degrades surprisingly faster than LM-PP in air. With only one MAH group on each PP chain for both LM-PP and HM-PP, the MAH density is much higher in LM-PP which generates a larger number of intermolecular hydrogen bonding that delays the

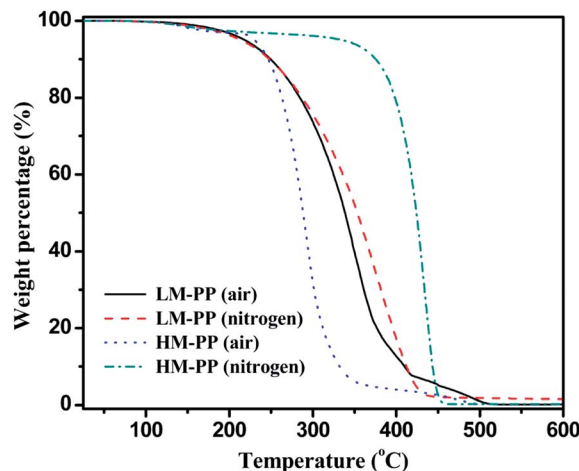


Fig. 6 TGA curves of pure LM-PP and HM-PP in air and nitrogen.

oxidative degradation of LM-PP. In nitrogen, thermal degradation becomes the only decomposition mechanism, and larger degradation temperature is observed from HM-PP due to the higher molecular weight. Fig. 7(a and b) show the degradation curves of pure PP, M-PP-PP blends and PNCs following the same heating procedures in air and nitrogen, respectively. In Fig. 7(a), pure PP shows the thermal decomposition temperature (T_d , recorded at 20% weight loss) at 270.6 °C in air, and the PP blends with LM-PP and HM-PP are observed to possess higher thermal stability, which reflects an increased T_d by 11.7 and 18.3 °C, respectively. After introducing 20 wt% NPs by the *in-situ* thermal decomposition method, the enhancement of the degradation temperature for the PNCs is much larger. The NPs-PP PNCs obtain the highest T_d of 388.2 °C, which is 117.6 °C higher than that of pure PP (270.6 °C). The NPs(LM-PP)-PP PNCs and NPs(HM-PP)-PP PNCs show their T_d at 378.6 and 332.6 °C, respectively. In order to disclose the nature of the NPs especially with a metal core in the decomposition of PP, the samples were also tested in a nitrogen flow condition. However, only slight thermal stability improvement is observed, Fig. 7(b), which is due to the strong particle-polymer interfacial interaction and is also observed in other polymer nanocomposite systems.^{9,40,66} The tremendous thermal stability improvement of around 117.6 °C as compared to pure PP is due to the presence of the NPs, especially with a metal core, as evidenced by Mössbauer spectra, Fig. 3. Iron acts as an oxygen trap and thus reduces the oxidation effect of oxygen on the PP molecular chains. The relatively poor thermal stability of NPs(HM-PP)-PP below 350 °C in air and 450 °C in nitrogen atmosphere is due to the poor interfacial compatibility between the HM-PP grafted NPs and PP matrix. Though a lot of nanomaterials such as carbon nanotubes^{67,68} and nanoclays^{69,70} have been used to improve the thermal stability of the polymers, still only limited enhancement (less than 50 °C) was observed in most of the reported observations. The unexpected high thermal stability in air of the PNCs synthesized from this *in-situ* method may provide some guidance to rational design oxygen trapping materials.

To remove the heat history effects induced by the prior hot press on the thermal properties, the DSC curves, Fig. 8 and 9, are recorded on the first cooling and second heating process. The

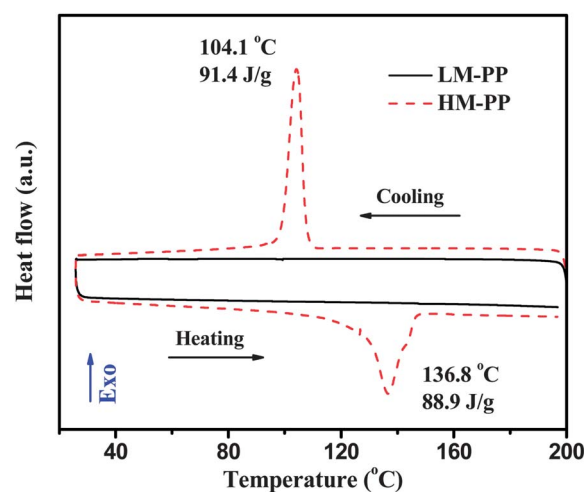


Fig. 8 DSC cooling (first cycle) and heating (second cycle) curves of LM-PP and HM-PP.

LM-PP and HM-PP show completely different DSC curves, Fig. 8. HM-PP exhibits strong melting and crystalline peaks during the heating and cooling process, respectively. However, no such peaks observed in LM-PP indicate its amorphous structure. These results are consistent with the concept that long chain PP molecules are preferred to be oriented and aligned, which enhances nucleation and causes crystal growth.⁷¹ In Fig. 9, all samples show a melting peak at around 150 °C. However, the crystalline peaks appear at different temperatures and the addition of LM-PP significantly shifts the peak to a lower temperature. The major peak of PP is maintained at 118 °C for HM-PP-PP blend and meanwhile a weak peak at ~106 °C shows up on the left shoulder of the major peak, which is from the crystallization of HM-PP. The lowered T_c for the PNCs, Fig. 9(d-f), is attributed to the strong interaction between the NPs and the polymer, which greatly restricts the segmental motion of the polymer chains and inhibits the patterning of the polymer chains to specific crystal structures.

Table 1 lists the DSC characteristics of the pure PP, LM-PP-PP, HM-PP-PP and their corresponding PNCs. The crystalline

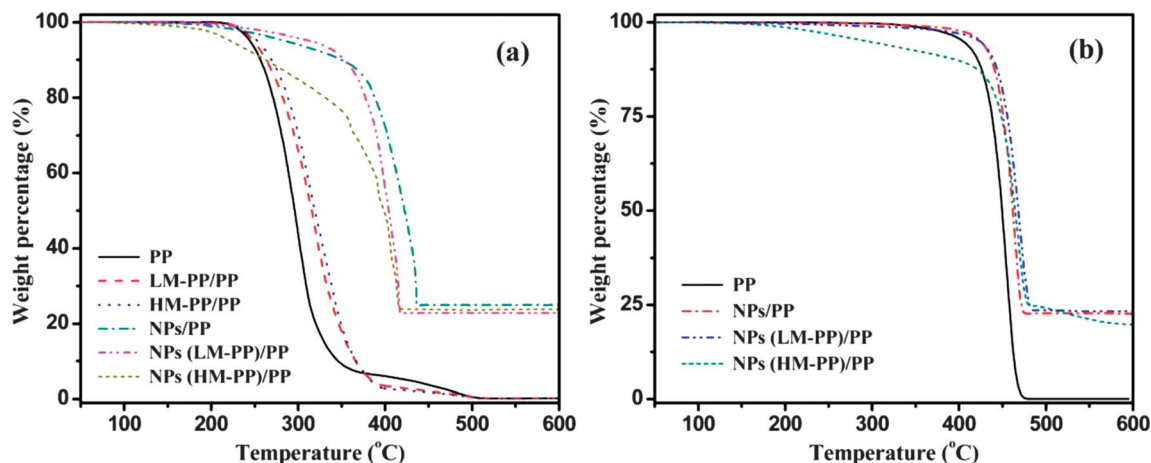


Fig. 7 TGA curves of pure PP, M-PP-PP blends, and PNCs in (a) air and (b) nitrogen.

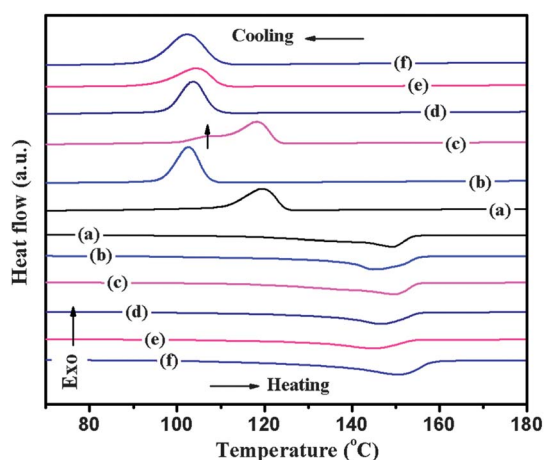


Fig. 9 DSC cooling (first cycle) and heating (second cycle) curves of (a) pure PP, (b) LM-PP-PP, (c) HM-PP-PP, (d) NPs-PP, (e) NPs(LM-PP)-PP and (f) NPs(HM-PP)-PP.

fraction (X_c) of PP within the blends or PNCs is calculated from eqn (1):

$$X_c = \frac{\Delta H}{209f_p} \quad (1)$$

where ΔH is the enthalpy of fusion (J g^{-1}), 209 is the fusion enthalpy for a theoretically 100% crystalline PP.⁷² And f_p is the weight fraction of PP excluding the weight of the NPs and M-PP. To calculate the crystallinity of PP for samples containing HM-PP, the contribution of the enthalpy of fusion from HM-PP is subtracted. The crystallinities of PP in M-PP-PP blends (LM-PP-PP: 44.1%, HM-PP-PP: 43.6%) are slightly higher than that of pure PP (43.3%), which arises from the heterogeneous nucleation effect of the M-PP molecules for initializing and accelerating the crystallization of the PP matrix.⁷³ For the PNCs, owing to the difference in conversion from $\text{Fe}(\text{CO})_5$ to iron NPs and the consequent oxidation degree, the nanoparticle fraction in the PNCs is calculated from the TGA and Mössbauer spectra results. First, the residue of the PNCs decomposed in air is obtained, which is 22.9, 23.8 and 25.0 wt% for NPs-PP, NPs(LM-PP)-PP and NPs(HM-PP)-PP (the final residue is Fe_2O_3), respectively; second, the Fe_2O_3 is converted to Fe%, which is 16.0, 16.6 and 17.5 wt%; finally, the actual weight loading of the NPs in each composition is calculated according to the different fractions of Fe, FeO and Fe_2O_3 species (from Mössbauer analysis) and 22.5, 23.6 and 20.0% is obtained for NPs-PP, NPs(LM-PP)-PP and NPs(HM-PP)-PP. Then the fraction of M-PP-PP in each composition is obtained for 77.5, 76.4 and 80.0 wt%, and also the fraction of M-PP (the weight ratio of M-PP : PP is fixed at 0.5 : 20) in NPs(LM-PP)-PP and NPs(HM-PP)-PP can be calculated as 1.86 and 1.95 wt%, respectively. The NPs(LM-PP)-PP exhibits an enhanced X_c by 7.5% as compared to pure PP, while NPs(HM-PP)-PP shows a dramatic decrease in X_c by 10.0%. The higher X_c of the NPs(LM-PP)-PP is arising from the more efficient crystalline behavior with the aid of the stabilized NPs. However, the lower X_c of the NPs(HM-PP)-PP is attributed to the fact that the long HM-PP polymer chains on the NPs surface are able to disturb the continuity of the polymer matrix and thus introduce more grain

boundaries as well as defects. Similar observations were reported previously in calcium carbonate-PP PNCs.²⁵ Recently, Rong *et al.* have shown that different polymers (styrene, methyl methacrylate, butyl acrylate, *et al.*) grafted SiO_2 NPs do not have a significant effect on the crystallinity of PP in composites,⁷⁴ implying that the M-PP would significantly affect the crystalline behavior of PP and also this behavior is molecular weight dependent.

3.4. Magnetic and electrical properties

Fig. 10 shows the room temperature magnetic hysteresis loops of PP PNCs with and without M-PP. The magnetization of the PNCs without M-PP is 6.1 emu g^{-1} at a magnetic field of 20 000 Oe (NPs loading is 20 wt%). PNCs at the same particle loading containing LM-PP are observed to obtain significantly larger magnetization of 19.6 emu g^{-1} , which is primarily due to the less oxidation of the NPs by a protective LM-PP layer covalently bonded to the NP surface. However, the PNCs containing HM-PP exhibit the lowest magnetization (saturated at low field) of 1.1 emu g^{-1} due to the almost complete oxidation of the NPs as evidenced by the Mössbauer spectra analysis, Fig. 3(c). The saturated magnetization of each composite is highly consistent with the results obtained from Mössbauer spectra analysis. The less oxidation of the NPs, the stronger magnetization of the composites since pure iron exhibits much higher saturated magnetization ($\sim 222 \text{ emu g}^{-1}$)^{75,76} than that of iron oxides ($\alpha\text{-Fe}_2\text{O}_3$: $\sim 1.2 \text{ emu g}^{-1}$, $\gamma\text{-Fe}_2\text{O}_3$: $\sim 64.0 \text{ emu g}^{-1}$ (ref. 78)). It is obvious that the hysteresis curves for the NPs-PP and NPs(LM-PP)-PP PNCs are not saturated even at the field of 20 000 Oe. The saturation magnetization (M_s) can be determined by the extrapolated saturation magnetization obtained from the intercept of magnetization *vs.* H^{-1} at high field.¹⁴ The M_s for NPs-PP and NPs(LM-PP)-PP PNCs are calculated to be 7.4 and 20.8 emu g^{-1} , respectively. The coercivity (H_c , the external applied magnetic field necessary to return the material to a zero magnetization condition) is less than 200 Oe for all three PNCs,

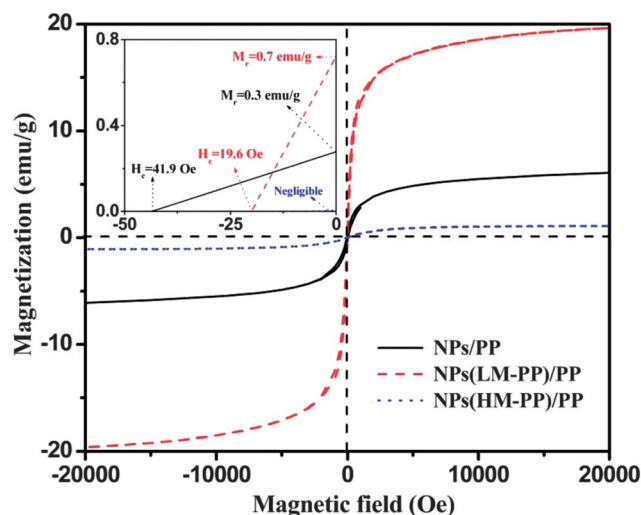


Fig. 10 Hysteresis loops of the NPs-PP, NPs(M-PP)-PP PNCs at room temperature. The inset shows enlarged hysteresis loops at low magnetic field to determine coercivity.

demonstrating soft ferromagnetic behavior. With the addition of LM-PP in the PNCs, the H_c is decreased from 41.9 to 19.6 Oe, indicating that the NPs(LM-PP)-PP PNCs are magnetically softer than NPs-PP PNCs. Moreover, the H_c approaches zero after introducing HM-PP in the PNCs, inset of Fig. 10. Very small remnant magnetization (M_r , the residue magnetization after the applied field is reduced to zero) is observed in each sample, which is 0.3 and 0.7 emu g⁻¹ for NPs-PP and NPs(LM-PP)-PP, respectively. The molecular weight of M-PP plays a significant role in protecting the NPs from oxidation and thus the final physicochemical performance of the PNCs. Especially, LM-PP can be used as a surfactant to effectively protect the *in-situ* produced NPs from oxidation, together with superior compatibility with the PP matrix, these organic-inorganic hybrids are of great potential to be successfully applied in various applications such as electronics and magnetic fluids.^{5,79,80}

The electrical resistivity (ρ) of the PNCs with and without M-PP is shown in Fig. 11. The PNCs without M-PP exhibit a ρ of $\sim 10^7 \Omega \text{ cm}$, 6 orders of magnitude lower than the pure PP.⁴⁰ By introducing LM-PP, the ρ decreased further by two orders of magnitude ($\sim 10^5 \Omega \text{ cm}$) due to the conductive NPs with less fraction of iron oxide. However, significantly larger ρ of about $10^{13} \Omega \text{ cm}$ is observed in the NPs(HM-PP)-PP PNCs due to the complete oxidation of the NPs. These observations are consistent with the Mössbauer spectra and magnetic property of the PNCs. Excluding the percolation effect since the same nanoparticle loading and similar nanoparticle size in these PNCs, the electron hopping between single NPs within these aggregates is much easier with a thinner oxide shell and thus resistivity is significantly reduced. For the completely oxidized NPs, more electrons are localized which results in larger resistivity.

4. Conclusion

The roles of maleic functionalized PP (M-PP) on the magnetic polypropylene nanocomposites prepared using an *in-situ* thermal decomposition method were studied. The molecular weights of M-PP were found to play a radical role in the physicochemical properties of the M-PP-PP blends and PNCs. The nanoparticle size was significantly influenced by an even introduction of a small amount of M-PP. A significantly decreased complex viscosity was observed after introducing M-PP, which is critically

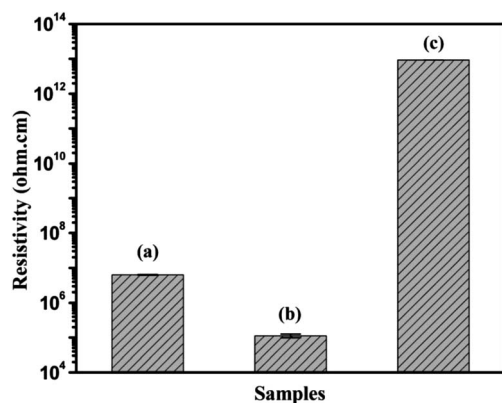


Fig. 11 Resistivity of (a) NPs-PP, (b) NPs(LM-PP)-PP, and (c) NPs(HM-PP)-PP.

important for the processing and manufacturing of PNCs. Mössbauer spectrum analysis revealed that the low molecular M-PP (LM-PP) enhanced the saturated magnetization of the PNCs indicating that the NPs are well protected from oxidation by the LM-PP shell and less affected by the surface oxidation effects. However, high molecular weight M-PP brought an almost complete oxidation of the nanoparticles and thus decreased magnetization and conductivity of the PNCs were observed. Thermal degradation results revealed a surprisingly high enhancement of the thermal stability by 117.6 °C in air due to the oxygen trapping effect of the NPs and the polymer-particle interaction. Both LM-PP and HM-PP promoted the crystallization of PP in the M-PP-PP blends. While in the PNCs, LM-PP increased the crystallinity of PP by 7.5% and HM-PP decreased the crystallinity of PP by 10.0% as compared to that of pure PP. The resistivity of the PNCs is consistent with the oxidation degree of the NPs that higher oxidation degree brought higher resistivity of the PNCs.

Acknowledgements

We acknowledge the supply of maleic functionalized polypropylene from Baker Hughes Plastics for this project. This project is partially supported by Baker Hughes Plastics and partial support from National Science Foundation – Chemical and Biological Separations (CBET: 11-37441) is also acknowledged. We appreciate support from the National Science Foundation – Nanoscale Interdisciplinary Research Team and Materials Processing and Manufacturing (CMMI 10-30755) to purchase TGA and DSC. D.P.Y. acknowledges support from the NSF under grant no. DMR 04-49022.

Notes and references

- Z. Guo, M. Moldovan, D. P. Young, L. L. Henry and E. J. Podlaha, *Electrochem. Solid-State Lett.*, 2007, **10**, E31–E35.
- W. Z. Li, S. S. Xie, L. X. Qian, B. H. Chang, B. S. Zou, W. Y. Zhou, R. A. Zhao and G. Wang, *Science*, 1996, **274**, 1701–1703.
- Z. Guo, S. Park, H. T. Hahn, S. Wei, M. Moldovan, A. B. Karki and D. P. Young, *Appl. Phys. Lett.*, 2007, **90**, 053111.
- G. Li, V. Joshi, R. L. White, S. X. Wang, J. T. Kemp, C. Webb, R. W. Davis and S. Sun, *J. Appl. Phys.*, 2003, **93**, 7557–7559.
- J.-H. Lee, Y.-M. Huh, Y.-w. Jun, J.-w. Seo, J.-t. Jang, H.-T. Song, S. Kim, E.-J. Cho, H.-G. Yoon, J.-S. Suh and J. Cheon, *Nat. Med.*, 2007, **13**, 95–99.
- A. K. Gupta and M. Gupta, *Biomaterials*, 2004, **26**, 3995–4021.
- Z. Guo, H. Lin, A. B. Karki, D. P. Young and H. T. Hahn, *Compos. Sci. Technol.*, 2008, **68**, 2551–2556.
- N. J. Tang, W. Chen, W. Zhong, H. Y. Jiang, S. L. Huang and Y. W. Du, *Carbon*, 2006, **44**, 423–427.
- J. Zhu, S. Wei, N. Haldolaarachchige, D. P. Young and Z. Guo, *J. Phys. Chem. C*, 2011, **115**, 15304–15310.
- J. Zhu, S. Wei, L. Zhang, Y. Mao, J. Ryu, N. Haldolaarachchige, D. P. Young and Z. Guo, *J. Mater. Chem.*, 2011, **21**, 3952–3959.
- X.-C. Sun and N. Nava, *Nano Lett.*, 2002, **2**, 765–769.
- Z. Guo, C. S. S. R. Kumar, L. L. Henry, E. E. Doomes, J. Hormes and E. J. Podlaha, *J. Electrochem. Soc.*, 2005, **152**, D1–D5.
- Y. Bao, H. Calderon and K. M. Krishnan, *J. Phys. Chem. C*, 2007, **111**, 1941–1944.
- Z. Guo, L. L. Henry, V. Palshin and E. J. Podlaha, *J. Mater. Chem.*, 2006, **16**, 1772–1777.
- J. Zhu, S. Wei, X. Chen, A. B. Karki, D. Rutman, D. P. Young and Z. Guo, *J. Phys. Chem. C*, 2010, **114**, 8844–8850.
- Z. Guo, T. Y. Kim, K. Lei, T. Pereira, J. G. Sugar and H. T. Hahn, *Compos. Sci. Technol.*, 2008, **68**, 164–170.

- 17 J. Zhu, S. Wei, D. Rutman, N. Haldolaarachchige, D. P. Young and Z. Guo, *Polymer*, 2011, **52**, 2947–2955.
- 18 P. Kim, N. M. Doss, J. P. Tillotson, P. J. Hotchkiss, M.-J. Pan, S. R. Marder, J. Li, J. P. Calame and J. W. Perry, *ACS Nano*, 2009, **3**, 2581–2592.
- 19 J. Zhu, S. Wei, M. J. Alexander, T. D. Dang, T. C. Ho and Z. Guo, *Adv. Funct. Mater.*, 2010, **20**, 3076–3084.
- 20 Z. Guo, S. Park, H. T. Hahn, S. Wei, M. Moldovan, A. B. Karki and D. P. Young, *J. Appl. Phys.*, 2007, **101**, 09M511.
- 21 J. Zhu, S. Wei, X. Chen, A. B. Karki, D. Rutman, D. P. Young and Z. Guo, *J. Phys. Chem. C*, 2010, **114**, 8844–8850.
- 22 Z. Guo, S. Park, S. Wei, T. Pereira, M. Moldovan, A. B. Karki, D. P. Young and H. T. Hahn, *Nanotechnology*, 2007, **18**, 335704.
- 23 B. Lin, G. A. Gelves, J. A. Haber, P. Pötschke and U. Sundararaj, *Macromol. Mater. Eng.*, 2008, **293**, 631–640.
- 24 J. Zhu, S. Wei, J. Ryu, M. Budhathoki, G. Liang and Z. Guo, *J. Mater. Chem.*, 2010, **20**, 4937–4948.
- 25 C.-M. Chan, J. Wu, J.-X. Li and Y.-K. Cheung, *Polymer*, 2002, **43**, 2981–2992.
- 26 Z. Guo, L. L. Henry and E. J. Podlaha, *ECS Trans.*, 2006, **1**, 63–69.
- 27 J. Zhu, S. Wei, A. Yadav and Z. Guo, *Polymer*, 2010, **51**, 2643–2651.
- 28 A. K. Kota, B. H. Cipriano, M. K. Duesterberg, A. L. Gershon, D. Powell, S. R. Raghavan and H. A. Bruck, *Macromolecules*, 2007, **40**, 7400–7406.
- 29 L. Shen, Y. Lin, Q. Du, W. Zhong and Y. Yang, *Polymer*, 2005, **46**, 5758–5766.
- 30 C. Lu and Y.-W. Mai, *Phys. Rev. Lett.*, 2005, **95**, 088303.
- 31 S. Barrau, P. Demont, C. Maraval, A. Bernes and C. Lacabanne, *Macromol. Rapid Commun.*, 2005, **26**, 390–394.
- 32 V. Favier, H. Chanzy and J. Y. Cavaille, *Macromolecules*, 1995, **28**, 6365–6367.
- 33 S. Stankovich, D. A. Dikin, G. H. B. Dommett, K. M. Kohlhaas, E. J. Zimney, E. A. Stach, R. D. Piner, S. T. Nguyen and R. S. Ruoff, *Nature*, 2006, **442**, 282–286.
- 34 A.-S. Robbes, J. Jestin, F. Meneau, F. Dalmás, O. Sandre, J. Perez, Fo. Boué and F. Cousin, *Macromolecules*, 2010, **43**, 5785–5796.
- 35 S.-P. Liu, J.-R. Ying, X.-P. Zhou, X.-L. Xie and Y.-W. Mai, *Compos. Sci. Technol.*, 2009, **69**, 1873–1879.
- 36 L. Sun, J. Liu, S. R. Kirumakki, E. D. Schwardtfefer, R. J. Howell, K. Al-Bahily, S. A. Miller, A. Clearfield and H.-J. Sue, *Chem. Mater.*, 2009, **21**, 1154–1161.
- 37 T. Kashiwagi, E. Grulke, J. Hilding, K. Groth, R. Harris, K. Butler, J. Shields, S. Kharchenko and J. Douglas, *Polymer*, 2004, **45**, 4227–4239.
- 38 S. Wei, R. Patil, L. Sun, N. Haldolaarachchige, X. Chen, D. P. Young and Z. Guo, *Macromol. Mater. Eng.*, 2011, **296**, 850–857.
- 39 Y. Li, J. Zhu, S. Wei, J. Ryu, L. Sun and Z. Guo, *Macromol. Chem. Phys.*, 2011, **212**, 1951–1959.
- 40 J. Zhu, S. Wei, Y. Li, L. Sun, N. Haldolaarachchige, D. P. Young, C. Southworth, A. Khasanov, Z. Luo and Z. Guo, *Macromolecules*, 2011, **44**, 4382–4391.
- 41 M. Sclavons, M. Laurent, J. Devaux and V. Carlier, *Polymer*, 2005, **46**, 8062–8067.
- 42 J. K. Mishra, J.-H. Ryou, G.-H. Kim, K.-J. Hwang, I. Kim and C.-S. Ha, *Mater. Lett.*, 2004, **58**, 3481–3485.
- 43 Z. P. Luo, *Acta Mater.*, 2006, **54**, 47–58.
- 44 F. Auriemma and C. De Rosa, *Macromolecules*, 2002, **35**, 9057–9068.
- 45 T. Foresta, S. Piccarolo and G. Goldbeck-Wood, *Polymer*, 2001, **42**, 1167–1176.
- 46 T. Kasuga, M. Hiramatsu, A. Hoson, T. Sekino and K. Niihara, *Adv. Mater.*, 1999, **11**, 1307–1311.
- 47 R. Hasegawa, Y. Aoki and M. Doi, *Macromolecules*, 1996, **29**, 6656–6662.
- 48 D. L. Green and J. Mewis, *Langmuir*, 2006, **22**, 9546–9553.
- 49 E. P. Giannelis, *Adv. Mater.*, 1996, **8**, 29–35.
- 50 C. Mikutta, R. Mikutta, S. Bonneville, F. Wagner, A. Voegelin, I. Christl and R. Kretschmar, *Geochim. Cosmochim. Acta*, 2008, **72**, 1111–1127.
- 51 V. M. Ugaz, D. K. Cinader and W. R. Burghardt, *Macromolecules*, 1997, **30**, 1527–1530.
- 52 J. M. Carella, J. T. Gotro and W. W. Graessley, *Macromolecules*, 1986, **19**, 659–667.
- 53 S. Wu, *Polymer*, 1987, **28**, 1144–1148.
- 54 A. V. Shenoy, *Rheology of Filled Polymer Systems*, Kluwer Academic Publishers, 1999.
- 55 A. C. Balazs, T. Emrick and T. P. Russell, *Science*, 2006, **314**, 1107–1110.
- 56 H. Münstedt, *Polym. Eng. Sci.*, 1981, **21**, 259–270.
- 57 L. A. Utracki and P. Sammut, *Polym. Eng. Sci.*, 1988, **28**, 1405–1415.
- 58 L. A. Utracki and P. Sammut, *Polym. Eng. Sci.*, 1990, **30**, 1027–1040.
- 59 T. D. Fornes, P. J. Yoon, H. Keskkula and D. R. Paul, *Polymer*, 2001, **42**, 09929–09940.
- 60 S. Sinha Ray, P. Maiti, M. Okamoto, K. Yamada and K. Ueda, *Macromolecules*, 2002, **35**, 3104–3110.
- 61 P. Pöschke, M. Abdel-Goad, I. Alig, S. Dudkin and D. Lellinger, *Polymer*, 2004, **45**, 8863–8870.
- 62 R. Krishnamoorti and E. P. Giannelis, *Macromolecules*, 1997, **30**, 4097–4102.
- 63 F. Du, R. C. Scogna, W. Zhou, S. Brand, J. E. Fischer and K. I. Winey, *Macromolecules*, 2004, **37**, 9048–9055.
- 64 X. Chen, S. Wei, A. Yadav, R. Patil, J. Zhu, R. Ximenes, L. Sun and Z. Guo, *Macromol. Mater. Eng.*, 2011, **296**, 434–443.
- 65 T. Kashiwagi, T. Hirata and J. E. Brown, *Macromolecules*, 1985, **18**, 131–138.
- 66 J. Zhu, S. Wei, R. Patil, D. Rutman, A. S. Kucknoor, A. Wang and Z. Guo, *Polymer*, 2011, **52**, 1954–1962.
- 67 J. J. Ge, H. Hou, Q. Li, M. J. Graham, A. Greiner, D. H. Reneker, F. W. Harris and S. Z. D. Cheng, *J. Am. Chem. Soc.*, 2004, **126**, 15754–15761.
- 68 T. Kashiwagi, F. Du, J. F. Douglas, K. I. Winey, R. H. Harris and J. R. Shields, *Nat. Mater.*, 2005, **4**, 928–933.
- 69 T. Agag, T. Koga and T. Takeichi, *Polymer*, 2001, **42**, 3399–3408.
- 70 J. Zhu, A. B. Morgan, F. J. Lamelas and C. A. Wilkie, *Chem. Mater.*, 2001, **13**, 3774–3780.
- 71 A. Nogales, B. S. Hsiao, R. H. Somani, S. Srinivas, A. H. Tsou, F. J. Balta-Calleja and T. A. Ezquerro, *Polymer*, 2001, **42**, 5247–5256.
- 72 Q. Yuan and R. D. K. Misra, *Polymer*, 2006, **47**, 4421–4433.
- 73 A. R. Bhattacharyya, T. V. Sreekumar, T. Liu, S. Kumar, L. M. Ericson, R. H. Hauge and R. E. Smalley, *Polymer*, 2003, **44**, 2373–2377.
- 74 M. Z. Rong, M. Q. Zhang, Y. X. Zheng, H. M. Zeng, R. Walter and K. Friedrich, *Polymer*, 2001, **42**, 167–183.
- 75 K. S. Suslick, M. Fang and T. Hyeon, *J. Am. Chem. Soc.*, 1996, **118**, 11960–11961.
- 76 N. A. D. Burke, H. D. H. Stöver and F. P. Dawson, *Chem. Mater.*, 2002, **14**, 4752–4761.
- 77 X.-M. Liu, S.-Y. Fu, H.-M. Xiao and C.-J. Huang, *J. Solid State Chem.*, 2005, **178**, 2798–2803.
- 78 B. R. V. Narasimhan, S. Prabhakar, P. Manohar and F. D. Gnanam, *Mater. Lett.*, 2002, **52**, 295–300.
- 79 P. Vacca, G. Nenna, R. Miscioscia, D. Palumbo, C. Minarini and D. D. Sala, *J. Phys. Chem. C*, 2009, **113**, 5777–5783.
- 80 A. F. Nogueira, B. S. Lomba, M. A. Soto-Oviedo, C. R. D. Correia, P. Corio, C. A. Furtado and I. A. Hümmelgen, *J. Phys. Chem. C*, 2007, **111**, 18431–18438.